Supplement of Geosci. Model Dev., 17, 5087–5121, 2024
https://doi.org/10.5194/gmd-17-5087-2024-supplement

Geoscientific Model Development
Open Access
EGU

Supplement of

Validating a microphysical prognostic stratospheric aerosol implementation in E3SMv2 using observations after the Mount Pinatubo eruption

Hunter York Brown et al.

Correspondence to: Hunter York Brown (hybrown@sandia.gov) and Benjamin Wagman (bmwagma@sandia.gov)

Relating mass and number to geometric mean diameter

Geometric mean diameter is related to mass and number through the following equations from table S1 in Liu et al. (2012):

$$D_g = \frac{D_{emit}}{\exp\left(\frac{3}{2}(\ln(\sigma_g))^2\right)}, \text{ Eq. S1}$$

Here, D_{emit}, or volume mean diameter, is defined by aerosol mass (E_{mass}) and number (E_{number})

$$D_{emit} = \left(\frac{E_{mass}}{\frac{\pi}{6}\rho E_{number}}\right)^{\frac{1}{3}}, \text{ Eq. S2}$$

Table S1: The different volcanic aerosol mode characteristics as well as the coarse mode dust and seasalt tuning factors used in the prognostic stratospheric aerosol models.

Model Version	**MAM4 aerosol size properties**	**Dust and seasalt emission tuning factors**
E3SMv2-PA	• Accumulation ○ $D_{gn,high}$: 0.44 µm ○ σ_g: 1.8 • Coarse ○ $D_{gn,high}$: 4.0 µm ○ $D_{gn,low}$: 1.0 µm ○ σ_g: 2.0	• dust_emis_factor = 1.5 • seasalt_emis_scale = 0.6
E3SMv2-SPA	• Accumulation ○ $D_{gn,high}$: 0.48 µm ○ σ_g: 1.6 • Coarse ○ $D_{gn,high}$: 40 µm ○ $D_{gn,low}$: 0.4 µm ○ σ_g: 1.2	• dust_emis_factor = 3.255 • seasalt_emis_scale = 0.36
CESM2-WACCM	• Accumulation ○ $D_{gn,high}$: 0.48 µm ○ σ_g: 1.6 • Coarse ○ $D_{gn,high}$: 40 µm ○ $D_{gn,low}$: 0.4 µm ○ σ_g: 1.2	• dust_emis_factor = 0.7 • seasalt_emis_scale = 0.9

Table S2: Aerosol properties from the 18 km WOPC and model comparison in Fig. 8. In this table, we diverge from the MAM4 naming convention of accumulation mode as the first mode, Aitken as the second mode, and coarse as the third mode – instead, we number them by increasing size. For the WOPC data, modes 1 and 2 are assumed to be accumulation and coarse, and for the models modes 1, 2, and 3 an are Aitken, accumulation, and coarse, respectively.

Date	**Source**	**Effective Radius**	**Mode**	**Dg**	**n(Dg)**	**Sigma**
19910419	WOPC	0.344±0.17	1	0.145±0.015	11.4±1.1	1.49
			2	0.918±0.09	0.7±0.07	1.05
	E3SMv2-PA	0.339	1	0.055	3.25	1.6
			2	0.145	3.93	1.8
			3	1.0	1.5×10^{-9}	2.0
	E3SMv2-SPA	0.318	1	0.052	2.25	1.6
			2	0.181	5.48	1.6
			3	0.711	0.02	1.2
	CESM2-WACCM		1	0.042	8.01	1.6
			2	0.172	7.39	1.6
			3	0.738	0.15	1.2
19910716	WOPC	0.332±0.09	1	0.077±0.008	9.8±1.0	2.14
	E3SMv2-PA	0.356	1	0.041	12.02	1.6
			2	0.154	5.08	1.8
			3	1.0	2.0×10^{-9}	2.0
	E3SMv2-SPA	0.328	1	0.037	11.1	1.6
			2	0.19	6.9	1.6
			3	0.79	0.03	1.2
	CESM2-WACCM		1	0.034	376.5	1.6
			2	0.163	22.0	1.6
			3	0.855	0.14	1.2
19911230	WOPC	0.882±0.31	1	0.361±0.04	18.2±1.8	1.27
			2	0.954±0.1	5.2±0.5	1.28
	E3SMv2-PA	0.992	1	0.052	0.02	1.6
			2	0.415	14.0	1.8
			3	1.1	1.2×10^{-9}	2.0
	E3SMv2-SPA	0.731	1	0.052	0.29	1.6
			2	0.271	17.8	1.6
			3	0.819	12.0	1.2
	CESM2-WACCM		1	0.059	0.25	1.6
			2	0.325	20.7	1.6
			3	0.909	21.5	1.2

19920508	WOPC	1.24±0.39	1	0.909±0.09	15.3±1.5	1.23
			2	1.92±0.19	2.8±0.3	1.09
	E3SMv2-PA	0.753	1	0.052	0.03	1.6
			2	0.316	9.5	1.8
			3	1.31	5.46×10^{-10}	2.0
	E3SMv2-SPA	0.8	1	0.052	0.09	1.6
			2	0.334	14.1	1.6
			3	0.828	19.76	1.2
	CESM2-WACCM		1	0.052	0.41	1.6
			2	0.352	13.48	1.6
			3	0.918	16.24	1.2
19920717	WOPC	1.12±0.53	1	0.46±0.05	11.9±1.2	1.35
			2	1.41±0.14	3.9±0.4	1.18
	E3SMv2-PA	0.71	1	0.052	0.26	1.6
			2	0.298	7.75	1.8
			3	1.21	7.1×10^{-10}	2.0
	E3SMv2-SPA	0.8	1	0.052	0.4	1.6
			2	0.343	11.8	1.6
			3	0.828	15.5	1.2
	CESM2-WACCM		1	0.041	1.29	1.6
			2	0.325	12.5	1.6
			3	0.936	10.9	1.2
19921218	WOPC	0.966±0.47	1	0.298±0.03	8.95±0.9	1.38
			2	0.99±0.1	6.3±0.6	1.23
	E3SMv2-PA	0.509	1	0.052	0.41	1.6
			2	0.217	6.09	1.8
			3	1.0	1.04×10^{-8}	2.0
	E3SMv2-SPA	0.761	1	0.052	0.15	1.6
			2	0.334	10.28	1.6
			3	0.79	12.1	1.2
	CESM2-WACCM		1	0.057	0.36	1.6
			2	0.343	9.7	1.6
			3	0.882	9.74	1.2
19930408	WOPC	0.808±0.39	1	0.684±0.07	15.1±1.5	1.28
			2	1.82±0.18	0.22±0.02	1.03
	E3SMv2-PA	0.441	1	0.057	0.84	1.6
			2	0.189	5.61	1.8
			3	1.1	7.83×10^{-10}	2.0

	E3SMv2-SPA	0.705	1	0.052	0.27	1.6
			2	0.298	8.96	1.6
			3	0.765	7.77	1.2
	CESM2-WACCM		1	0.048	1.82	1.6
			2	0.298	9.31	1.6
			3	0.873	5.77	1.2
19930621	WOPC	0.866±0.39	1	0.244±0.02	13.8±1.4	1.47
			2	1.1±0.11	2.2±0.2	1.22
	E3SMv2-PA	0.467	1	0.05	3.99	1.6
			2	0.199	5.83	1.8
			3	1.0	1.9×10^{-9}	2.0
	E3SMv2-SPA	0.687	1	0.05	1.68	1.6
			2	0.289	8.77	1.6
			3	0.774	5.4	1.2
	CESM2-WACCM		1	0.037	6.5	1.6
			2	0.253	10.9	1.6
			3	0.927	3.23	1.2
19931116	WOPC	0.757±0.37	1	0.334±0.03	6.48±0.6	1.42
			2	0.95±0.1	1.95±0.2	1.2
	E3SMv2-PA	0.361	1	0.057	1.15	1.6
			2	0.154	4.43	1.8
			3	1.92	1.0×10^{-10}	2.0
	E3SMv2-SPA	0.62	1	0.052	0.24	1.6
			2	0.262	6.66	1.6
			3	0.711	3.71	1.2
	CESM2-WACCM		1	0.052	1.18	1.6
			2	0.262	7.12	1.6
			3	0.81	3.03	1.2

Table S3: Comparison of absorption efficiency at 10 μm from CESM2-WACCM model simulations given different complex refractive index assumptions. The complex refractive index n_{Hess} is akin to assuming no aerosol water (i.e., pure sulfate), while n_s includes the volume weighted contributions from n_{Hess} and n_{wat}.

Date	Region	Q_a (n_{Hess}, w/o water)	Q_a (n_s, volume-weighted water and sulfate)	% Difference ($(Q_{a,ns}-Q_{a,nhess})/Q_{a,ns}$)
1991-04	41˚N	0.055	0.048	-14.6
	20˚S–20˚N	0.087	0.077	-13
1991-07	41˚N	0.1	0.083	-20.5
	20˚S–20˚N	0.104	0.092	-13.0
1991-12	41˚N	0.163	0.138	-18.1
	20˚S–20˚N	0.178	0.156	-14.1
1992-04	41˚N	0.167	0.14	-19.3
	20˚S–20˚N	0.177	0.155	-14.2
1992-07	41˚N	0.163	0.137	-19.0
	20˚S–20˚N	0.175	0.154	-13.6
1992-12	41˚N	0.157	0.131	-19.8
	20˚S–20˚N	0.168	0.146	-15.1
1993-04	41˚N	0.14	0.12	-16.7
	20˚S–20˚N	0.16	0.139	-15.1
1993-07	41˚N	0.13	0.109	-19.3
	20˚S–20˚N	0.15	0.131	-14.5
1993-12	41˚N	0.116	0.099	-17.2
	20˚S–20˚N	0.152	0.129	-17.8

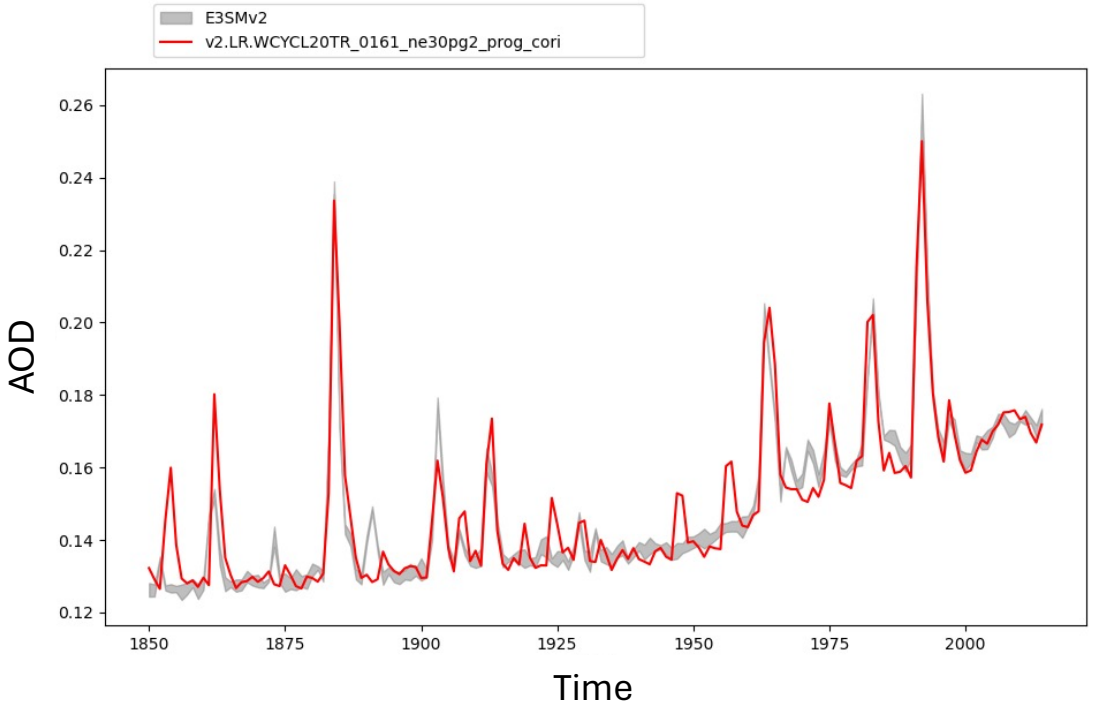

Fig. S1: Total aerosol optical depth (AOD) from an E3SMv2 stratospheric prognostic aerosol (SPA) fully coupled simulation from 1850-2014 (initialized from year 50 of a 100-year pre-industrial spin-up simulation) compared to a five-member ensemble of E3SMv2 historical simulations with prescribed volcanic forcing from Phase 6 of the Coupled Model Intercomparison Project (CMIP6; (Golaz et al., 2022)). We are plotting annual averages, and the gray shading shows the range in annual averages of the 5 ensemble members.

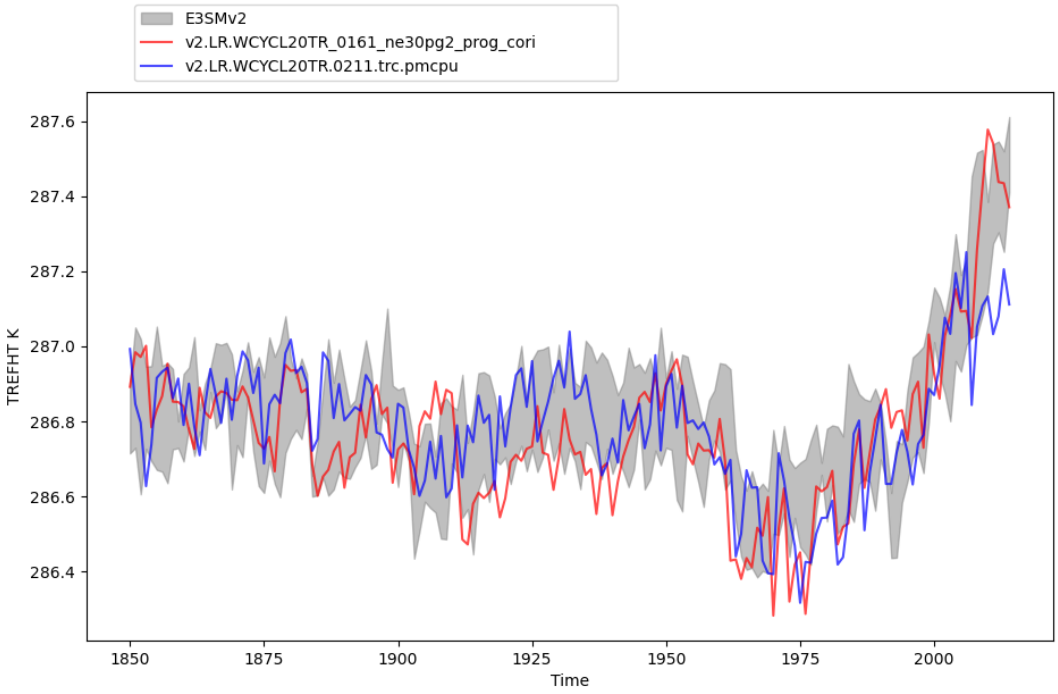

Fig. S2: Reference height (2 meter) temperature (˚K) from two E3SMv2 stratospheric prognostic aerosol (SPA) fully coupled simulations from 1850-2014 (initialized from years 50 and 100 of a 100-year pre-industrial spin-up simulation) compared to a five-member ensemble of E3SMv2 historical simulations with prescribed volcanic forcing from Phase 6 of the Coupled Model Intercomparison Project (CMIP6; (Golaz et al., 2022)). We are plotting annual averages, and the gray shading shows the range in annual averages of the 5 ensemble members.

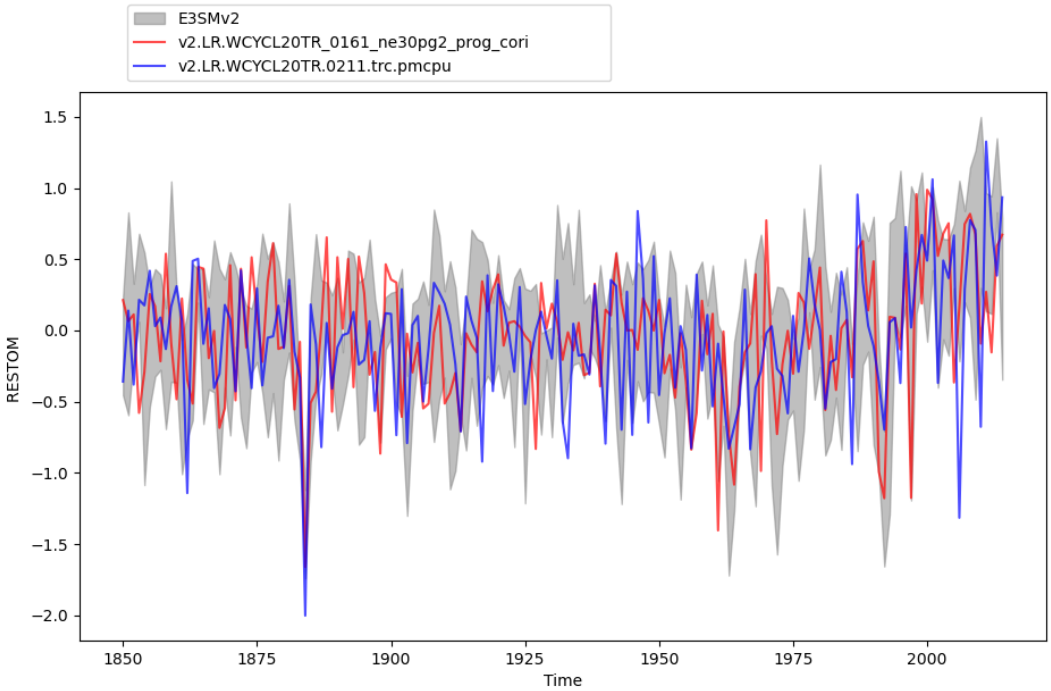

Fig. S3: Net radiative balance at the top-of-model (RESTOM) from two E3SMv2 stratospheric prognostic aerosol (SPA) fully coupled simulations from 1850-2014 (initialized from years 50 and 100 of a 100-year pre-industrial spin-up simulation) compared to a five-member ensemble of E3SMv2 historical simulations with prescribed volcanic forcing from Phase 6 of the Coupled Model Intercomparison Project (CMIP6; (Golaz et al., 2022)). We are plotting annual averages, and the gray shading shows the range in annual averages of the 5 ensemble members.

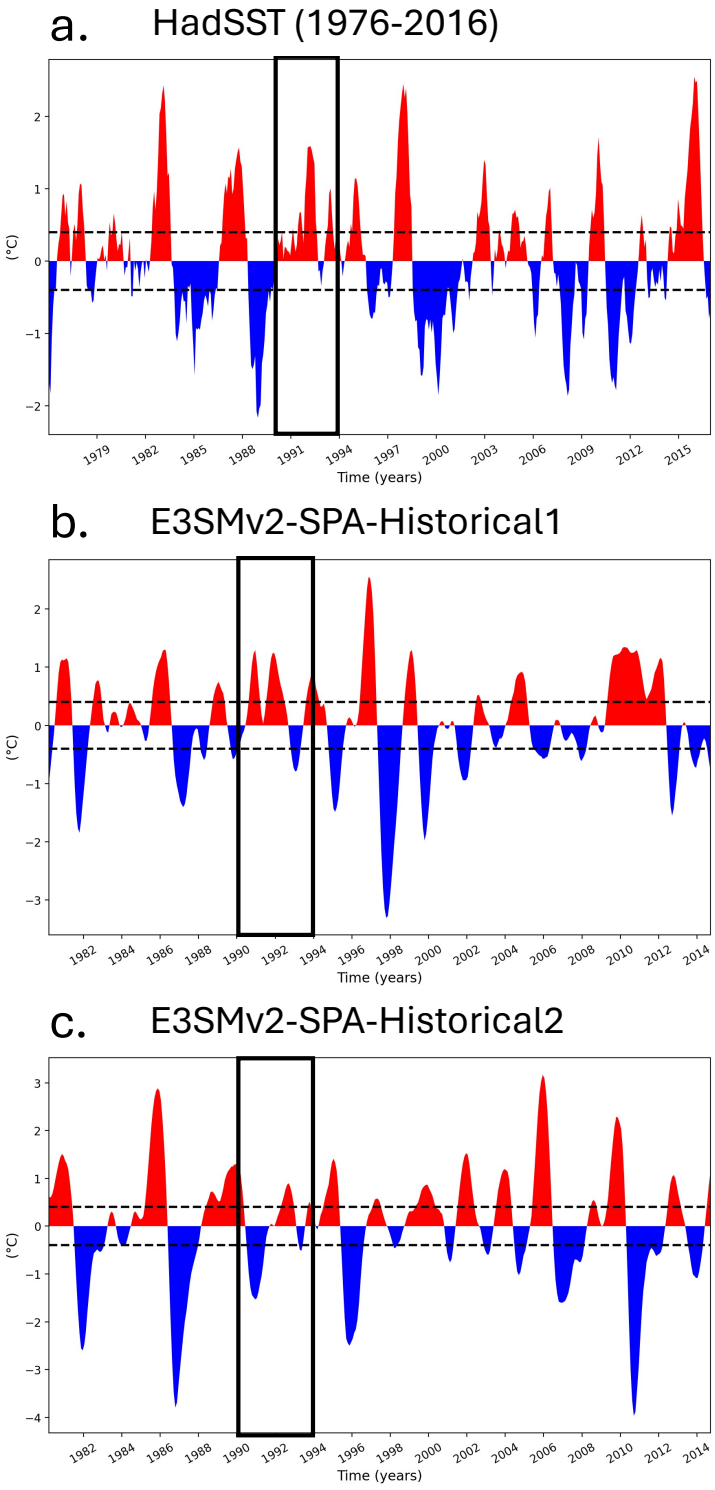

Fig. S4: Niño 3.4 index for the Met Office Hadley Center sea surface temperature dataset (HadSST; Kennedy et al., 2019) and the two E3SMv2 stratospheric prognostic aerosol (SPA) fully coupled ensembles from 1850-2014 (initialized from years 50 and 100 of a 100-year pre-industrial spin-up simulation). This index is a 5-month running mean of SST anomalies (relative to the period 1950-1979) over the Niño 3.4 region (5˚N-5˚S, 120˚-170˚W) (Trenberth, 1997). It is

considered an El Niño event if the anomalies exceed 0.4˚C, and it is considered an El Niña event if they surpass -0.4˚C (dotted lines). Boxed regions indicate the 1990-1994 period corresponding to pre- and post-Pinatubo eruption. These plots were output from the E3SM diagnostic package.

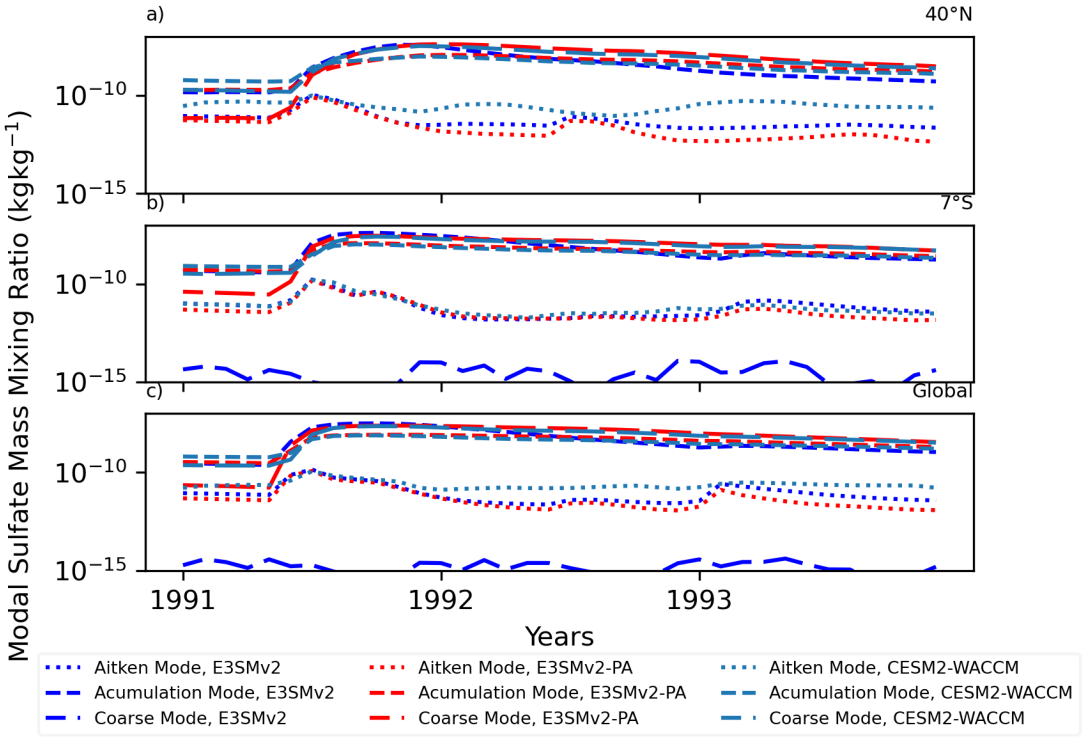

Figure S5: Modal sulfate interstitial mass (kg kg^{-1}) for the UARS regions (40˚N and 7˚S latitude bands; <=100 hPa) and globally averaged (<=100 hPa). Sulfate modal mass reported for Aitken (dotted), accumulation (dashed), and coarse modes (long dash).

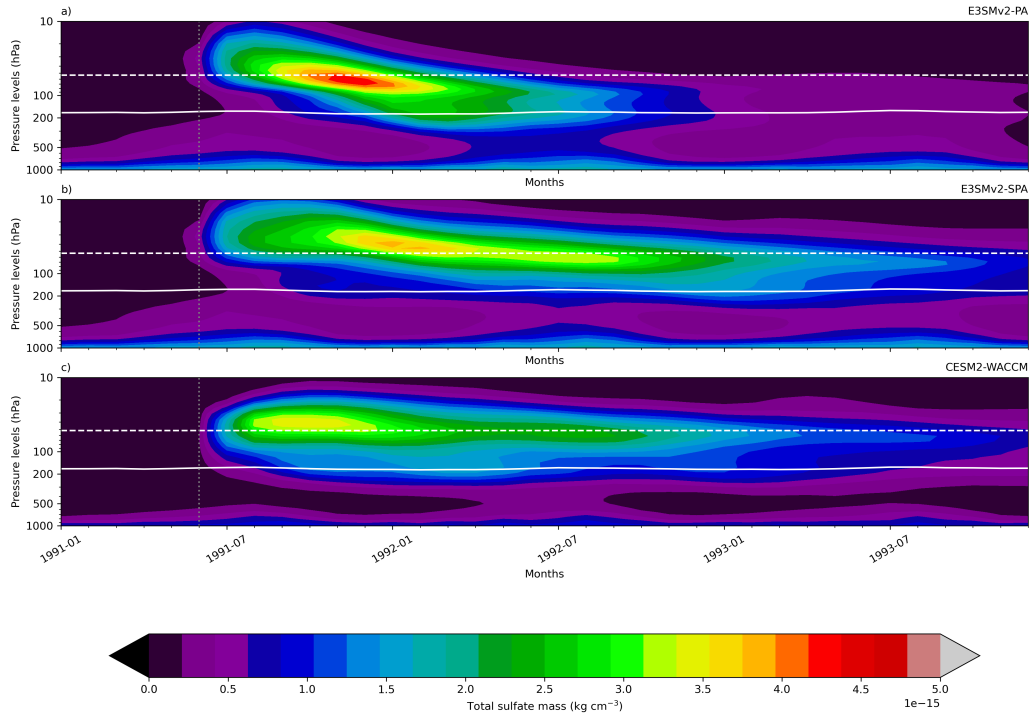

Figure S6: Vertical distribution of global mean sulfate aerosol mass concentration from 1991-1993 for (a) E3SMv2-PA, (b) E3SMv2-SPA, and (c) CESM2-WACCM. The solid white line denotes the average model tropopause. The dashed white line denotes the nearest model level to the 20 km geopotential height level, globally averaged. The vertical dotted gray line marks the Pinatubo eruption.

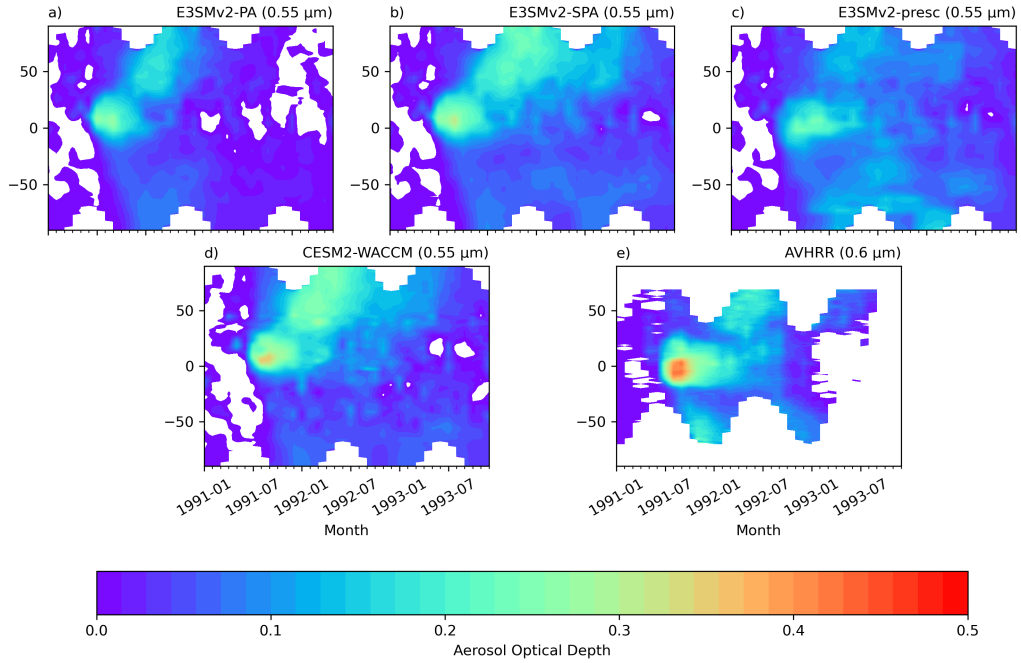

Figure S7: Same as Fig. 3 in text, except removing the land and missing-AVHRR-data masks that were used to improve comparability between models and AVHRR.

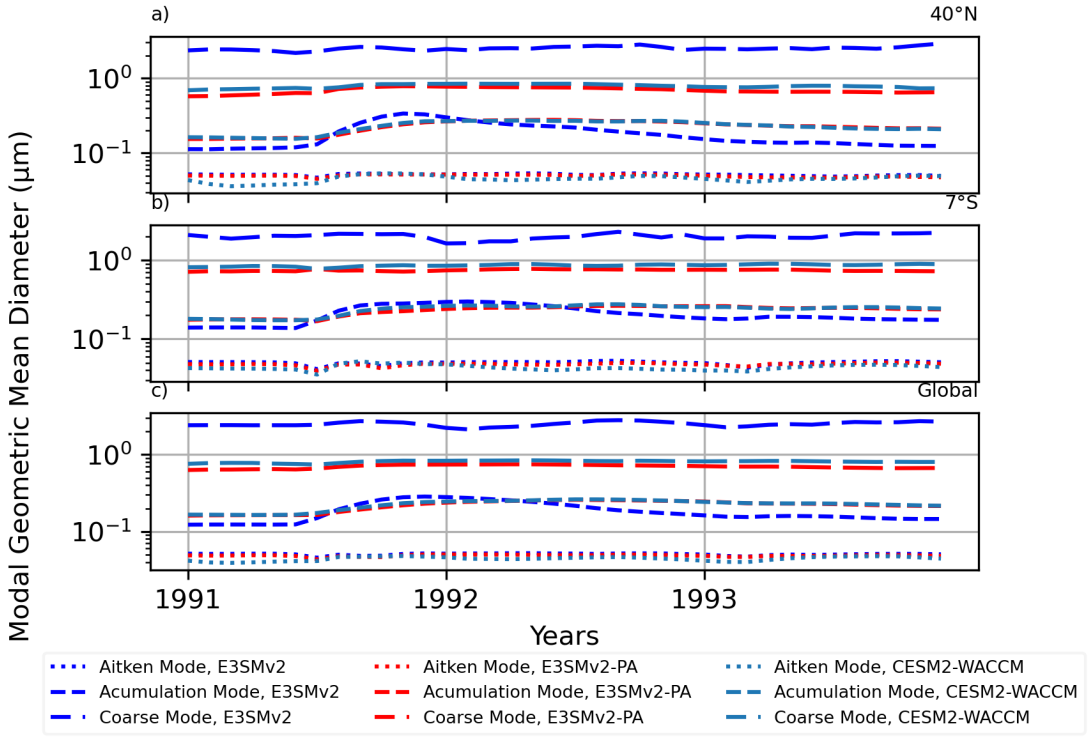

Figure S8: Modal aerosol diameters (μm) for the UARS regions (40˚N and 7˚S latitude bands; <=100 hPa) and globally averaged (<=100 hPa). Geometric mean diameters reported for Aitken (dotted), accumulation (dashed), and coarse modes (long dash).

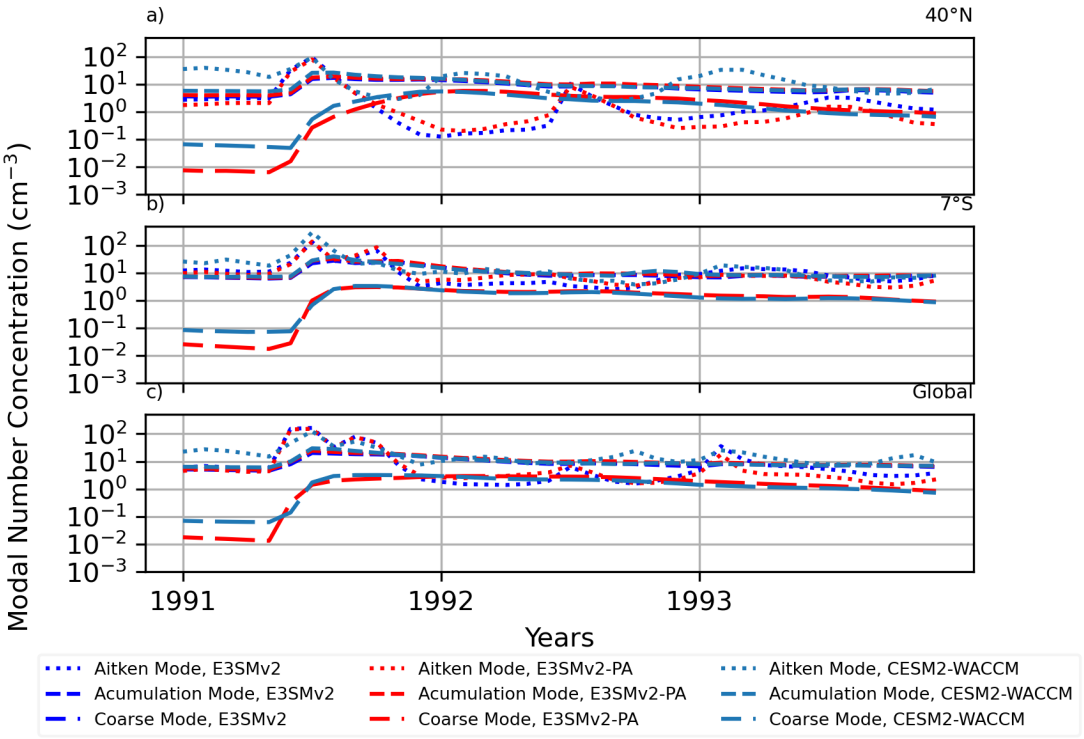

Figure S9: Modal aerosol number concentrations (cm^{-3}) for the UARS regions (40˚N and 7˚S latitude bands; <=100 hPa) and globally averaged (<=100 hPa). Geometric mean diameters reported for Aitken (dotted), accumulation (dashed), and coarse modes (long dash).

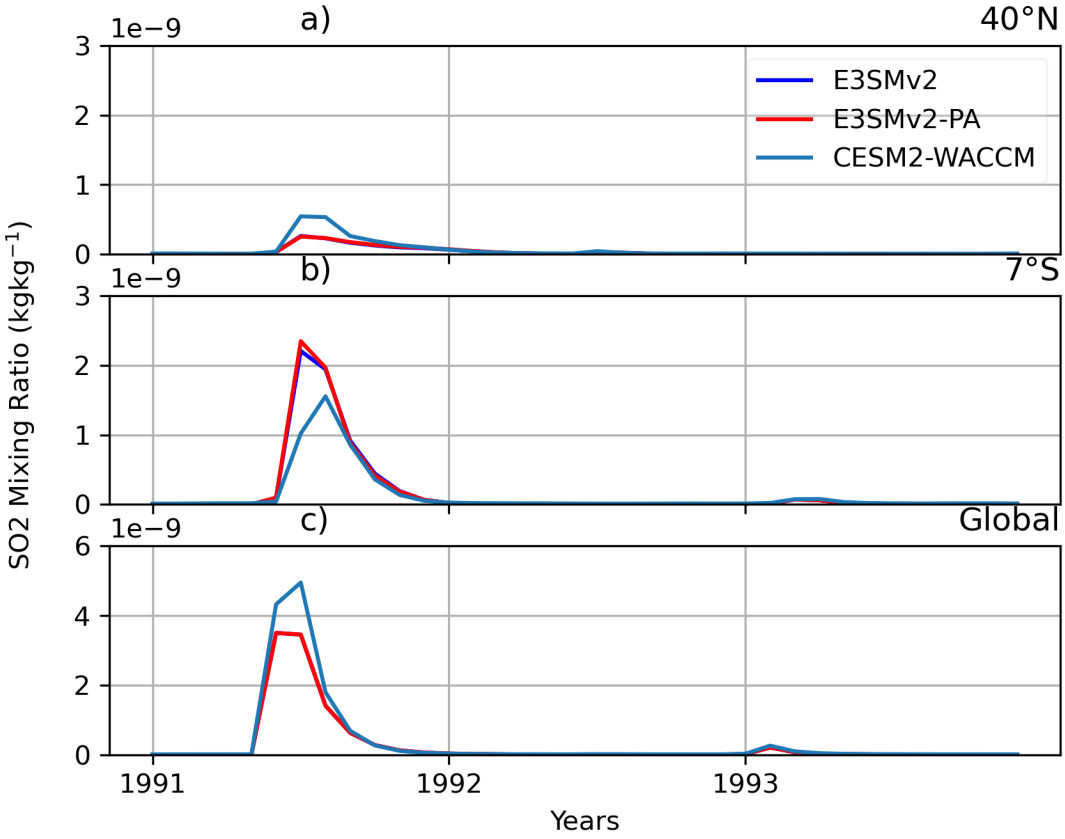

Figure S10 Sulfur dioxide mass mixing ratio (kg kg^{-1}) for the UARS regions (40˚N and 7˚S latitude bands; <=100 hPa) and globally averaged (<=100 hPa).

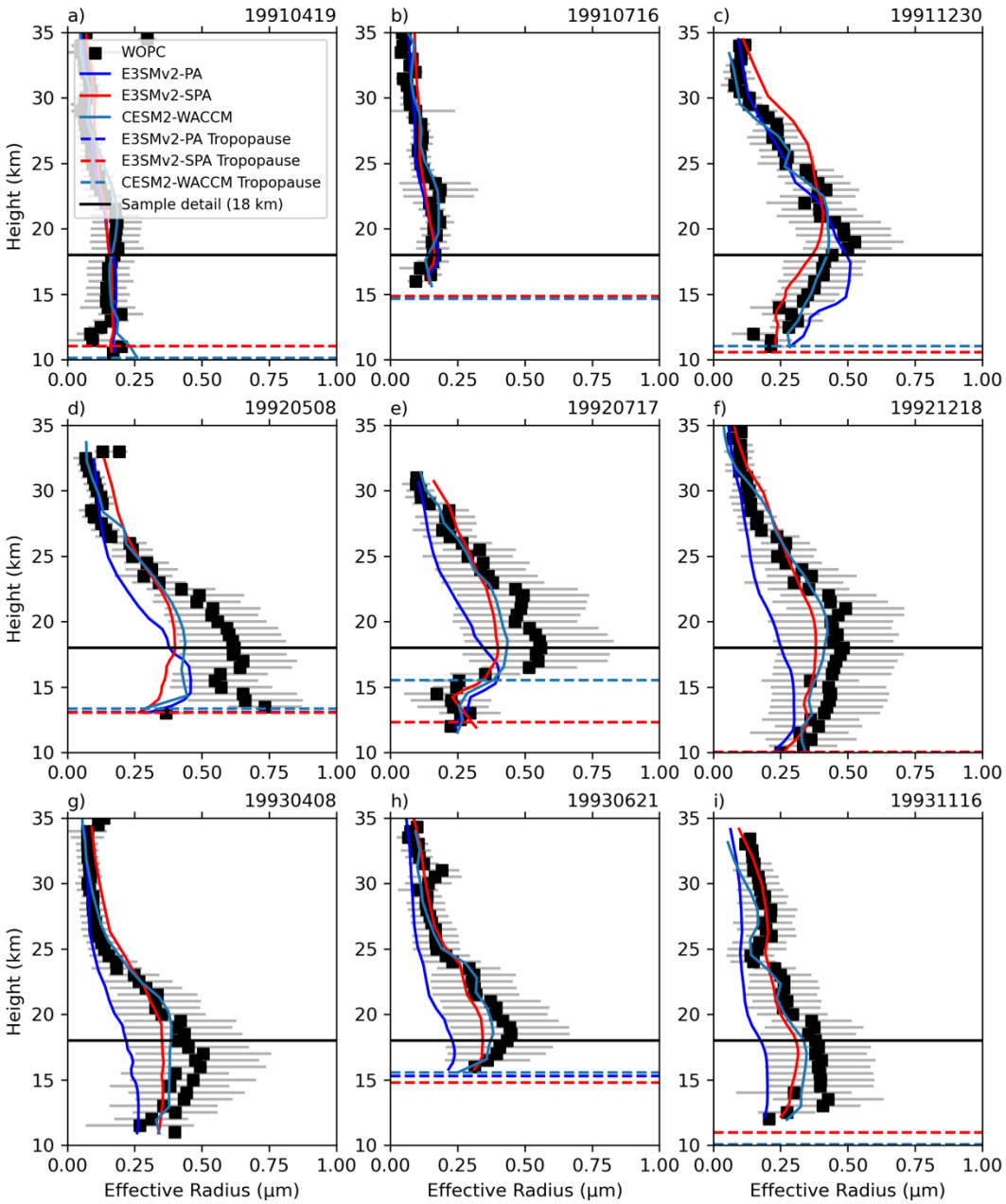

Figure S11: Vertical profiles of daily WOPC samples over Laramie (41˚N 105˚W) compared to E3SM and CESM2-WACCM. Dashed lines show the model tropopause and the solid black line marks the 18 km sample level corresponding to size distributions in Fig. 8. Results are for a single grid cell.

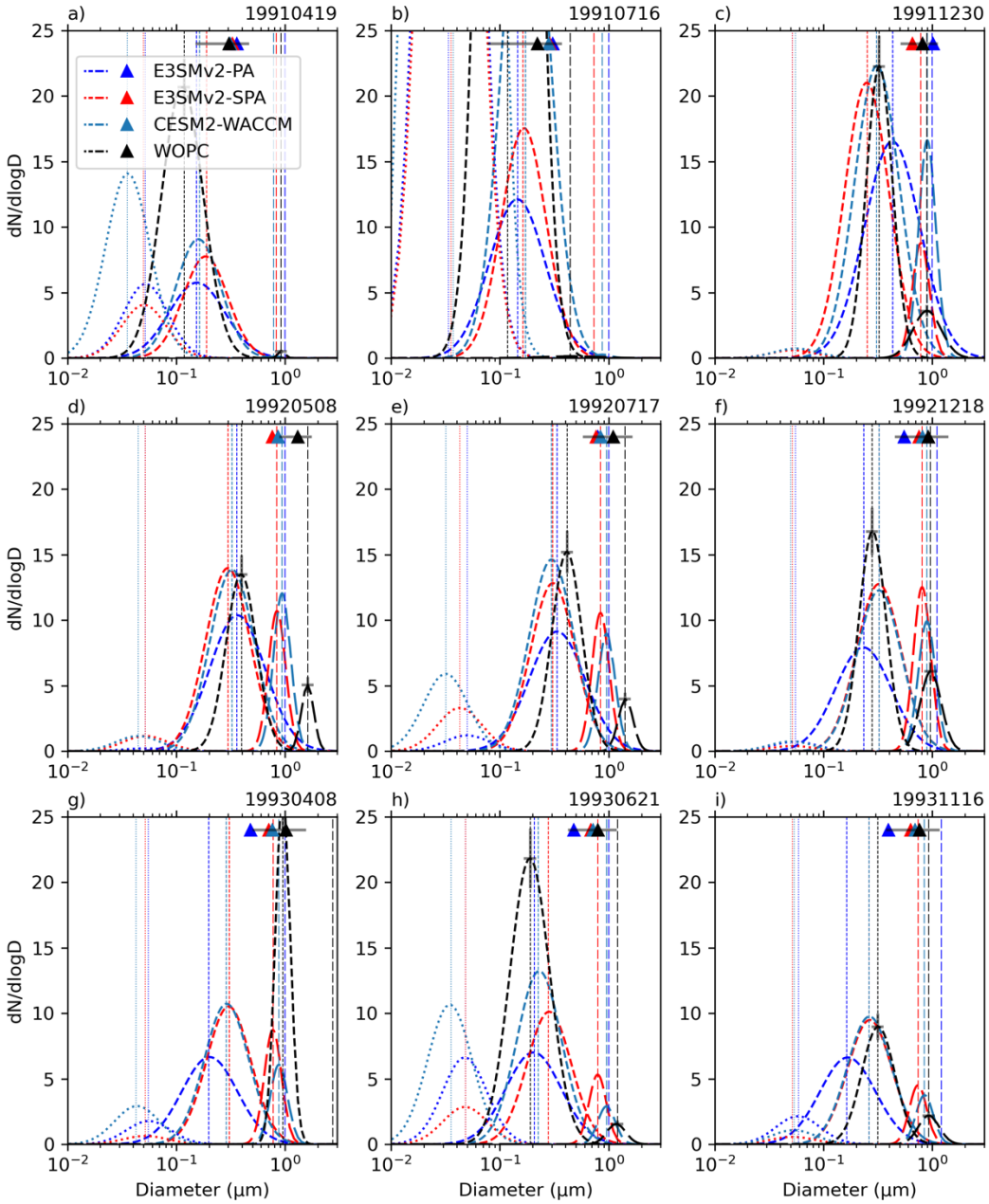

Figure S12: Same as Fig. 8, but for a 17 km sample level.

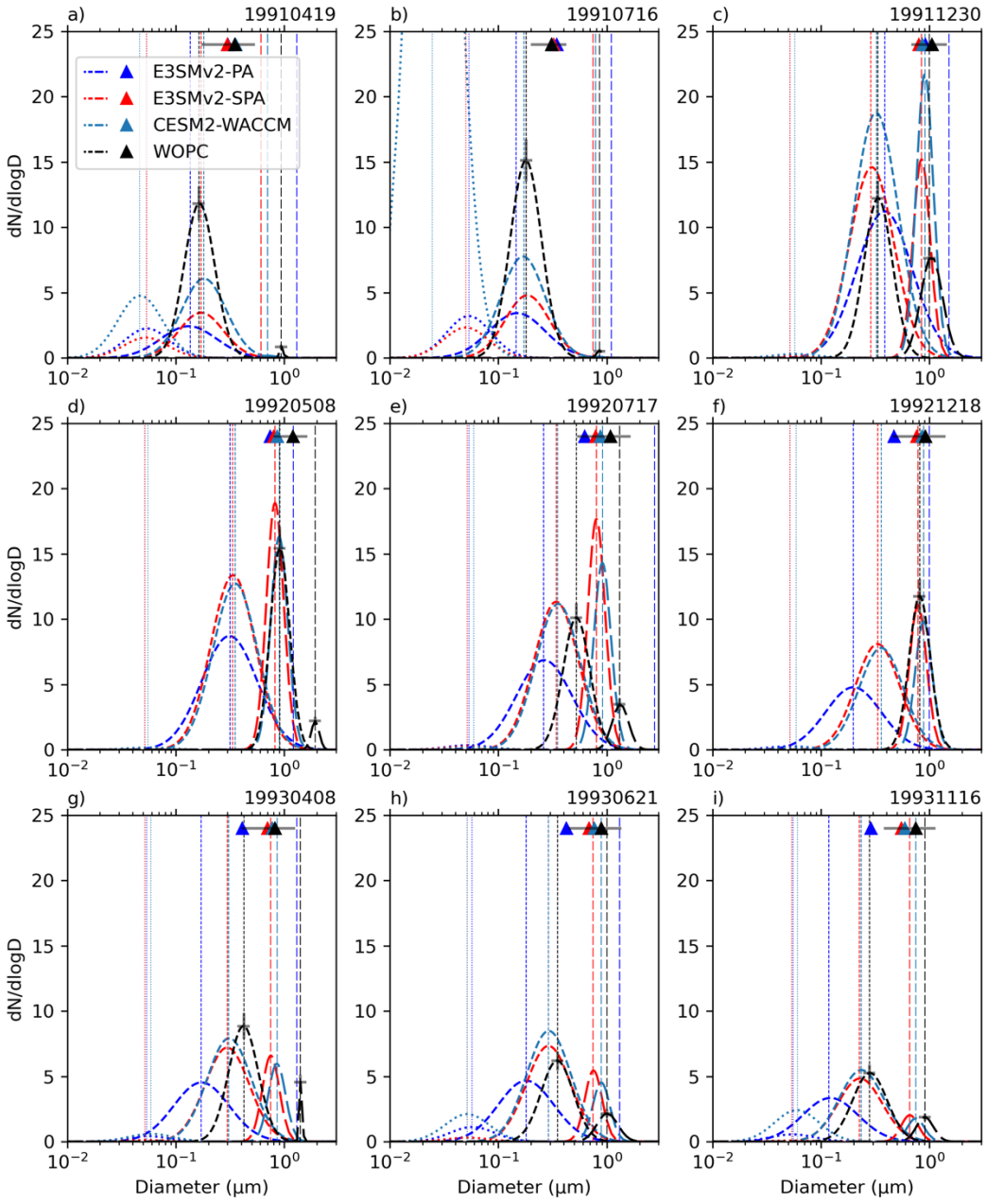

Figure S13: Same as Fig. 8, but for a 19 km sample level.

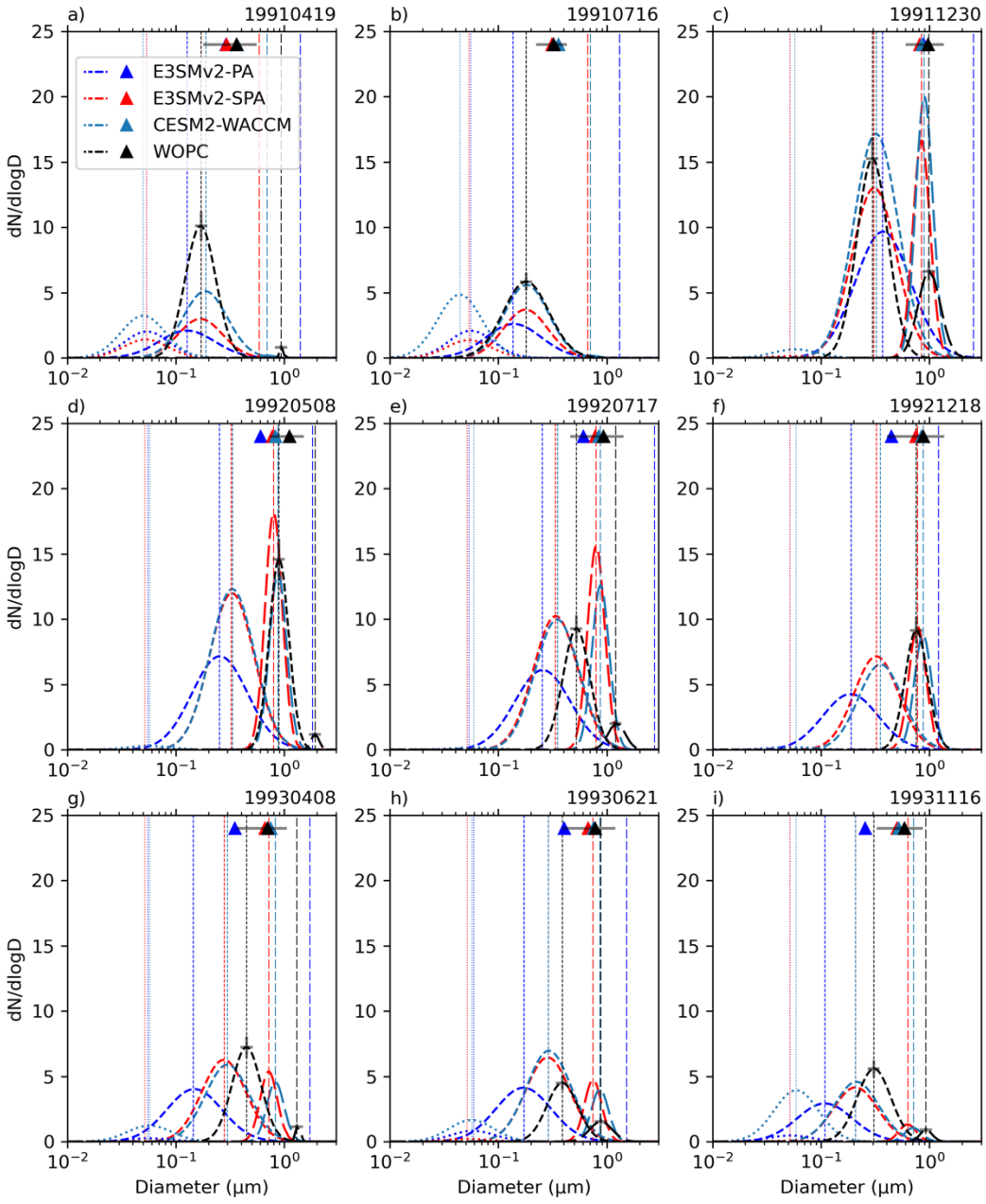

Figure S14: Same as Fig. 8, but for a 20 km sample level.

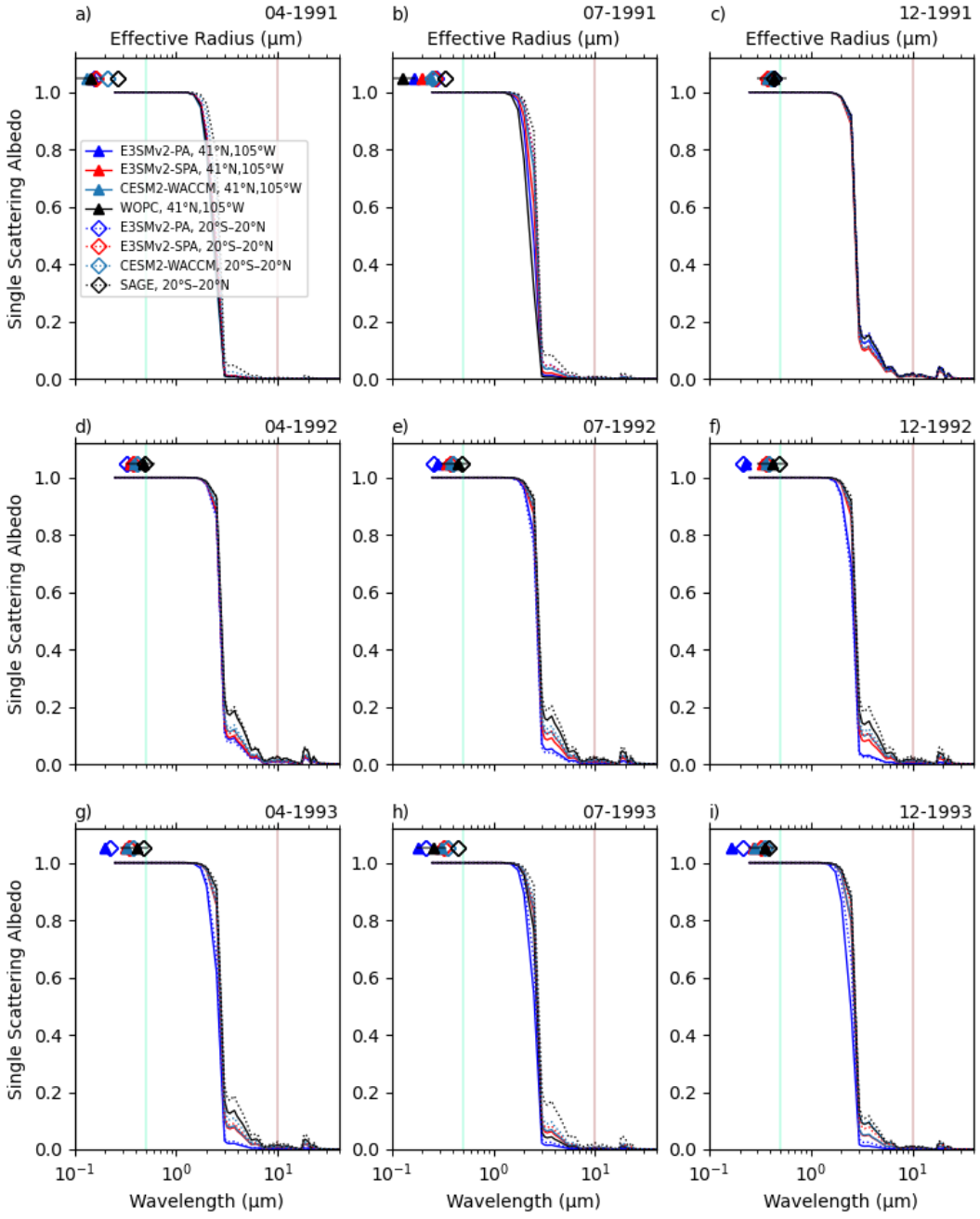

Figure S15: Single scattering albedo (SSA) calculated from effective radii and Hess et al. (1998) 0% RH sulfate refractive index. SSA is the ratio of the scattering and extinction efficiencies (Q_s/Q_e). Same sample regions as Figure 7: WOPC (41˚N 105˚W; 130-10 hPa) and SAGE (20˚S-20˚ N; 50-10 hPa). The turquoise vertical line marks the solar black body wavelength of maximum

irradiance (0.5 µm) and the dark red line marks the terrestrial black body wavelength of maximum irradiance (10 µm).

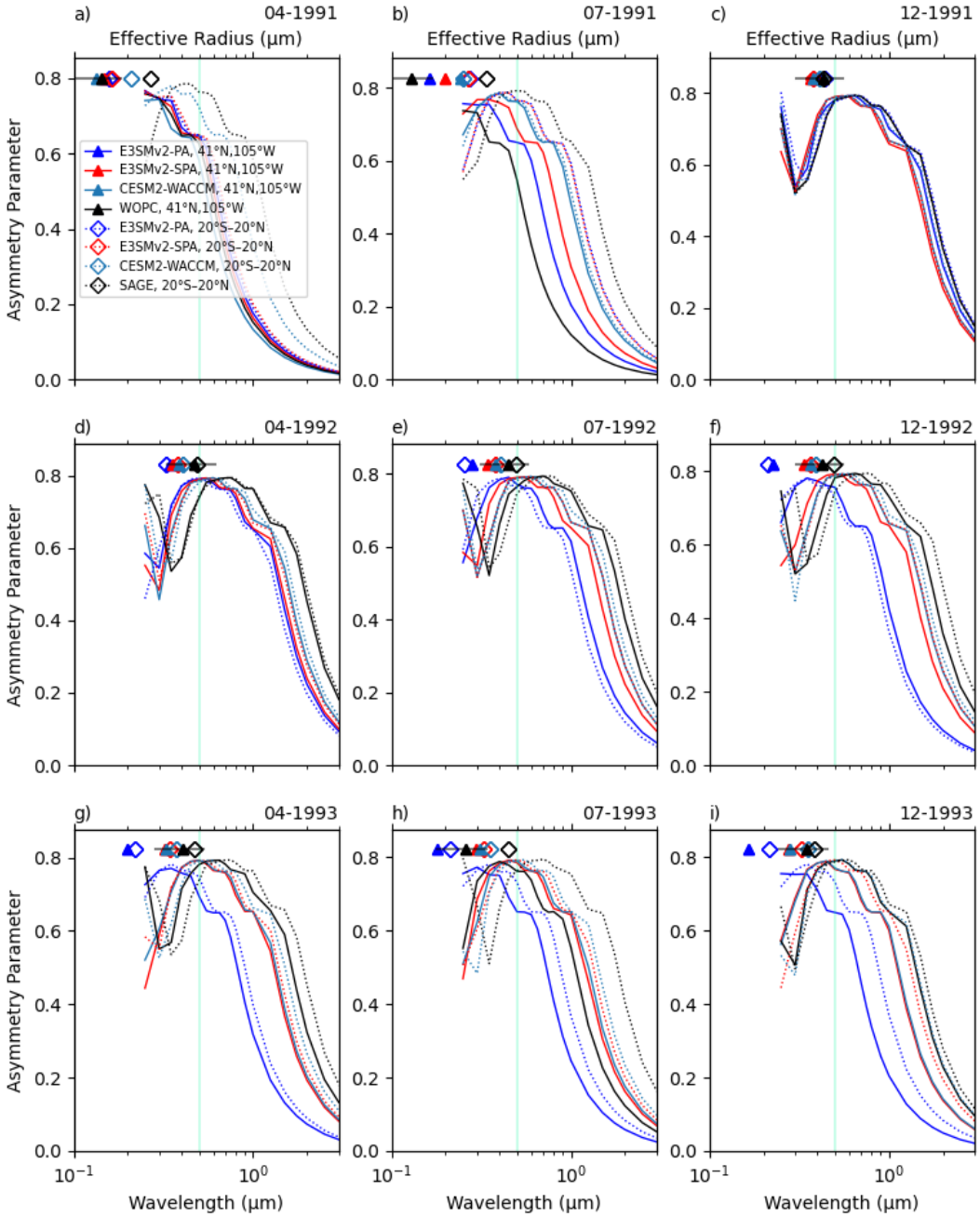

Figure S16: Asymmetry parameter (g) calculated from effective radii and Hess et al. (1998) 0% RH sulfate refractive index. The g is the intensity-weighted cosine of the scattering angle and ranges from 1 – -1, where g=1 is forward scattering, g=0 is isotropic scattering, and g=-1 is back scattering. Same sample regions as Figure 7: WOPC (41˚N 105˚W; 130-10 hPa) and SAGE (20˚S-20˚N; 50-10 hPa). The turquoise vertical line marks the solar black body wavelength of maximum irradiance (0.5 µm) and the dark red line marks the terrestrial black body wavelength of maximum irradiance (10 µm).

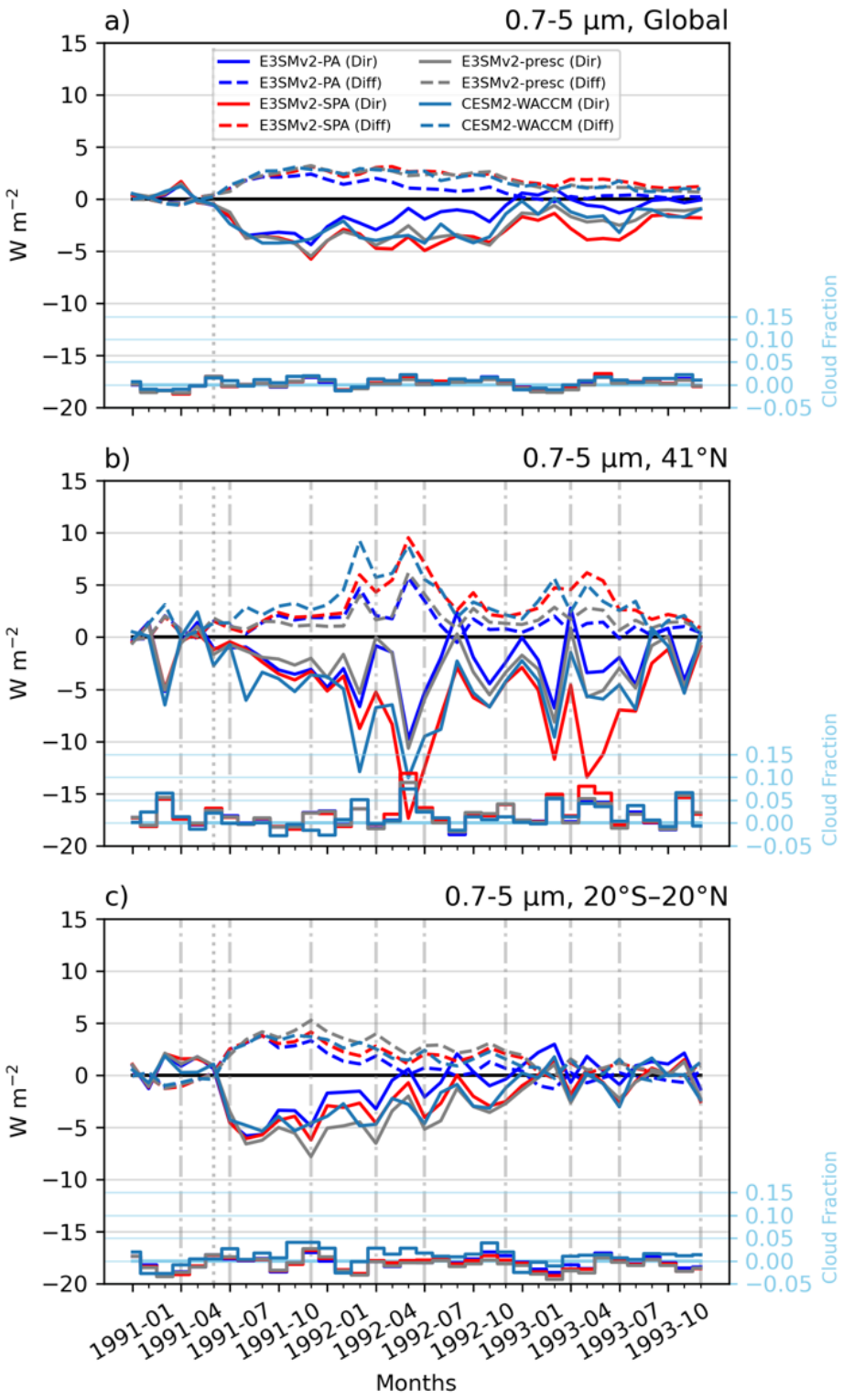

Figure S17: Same as Fig. 11 but for 0.7-5 µm wavelengths.

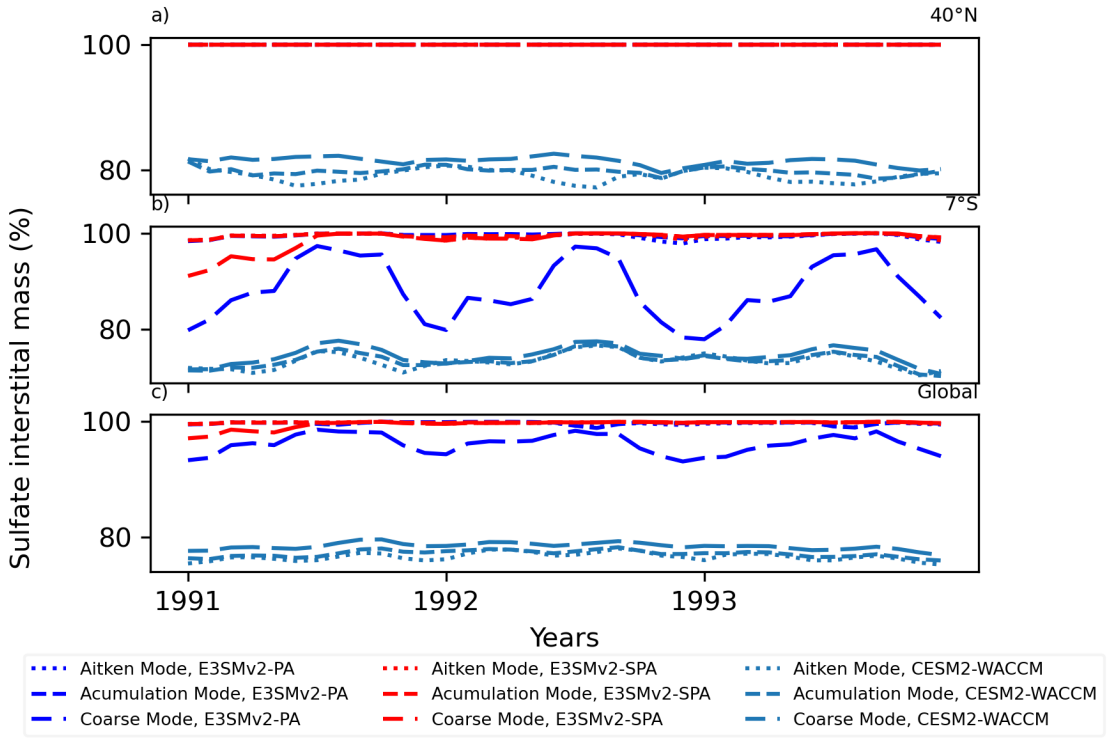

Figure S18: Percent of total mass (interstitial sulfate + interstitial water) composed of sulfate in the stratosphere for 40˚N, 7˚S, and global averages.

References:
Golaz, J., Van Roekel, L. P., Zheng, X., Roberts, A. F., Wolfe, J. D., Lin, W., Bradley, A. M., Tang, Q., Maltrud, M. E., Forsyth, R. M., Zhang, C., Zhou, T., Zhang, K., Zender, C. S., Wu, M.,

Wang, H., Turner, A. K., Singh, B., Richter, J. H., Qin, Y., Petersen, M. R., Mametjanov, A., Ma, P., Larson, V. E., Krishna, J., Keen, N. D., Jeffery, N., Hunke, E. C., Hannah, W. M., Guba, O., Griffin, B. M., Feng, Y., Engwirda, D., Di Vittorio, A. V., Dang, C., Conlon, L. M., Chen, C., Brunke, M. A., Bisht, G., Benedict, J. J., Asay-Davis, X. S., Zhang, Y., Zhang, M., Zeng, X., Xie, S., Wolfram, P. J., Vo, T., Veneziani, M., Tesfa, T. K., Sreepathi, S., Salinger, A. G., Reeves Eyre, J. E. J., Prather, M. J., Mahajan, S., Li, Q., Jones, P. W., Jacob, R. L., Huebler, G. W., Huang, X., Hillman, B. R., Harrop, B. E., Foucar, J. G., Fang, Y., Comeau, D. S., Caldwell, P. M., Bartoletti, T., Balaguru, K., Taylor, M. A., McCoy, R. B., Leung, L. R., and Bader, D. C.: The DOE E3SM Model Version 2: Overview of the Physical Model and Initial Model Evaluation, J Adv Model Earth Syst, 14, https://doi.org/10.1029/2022MS003156, 2022.

Hess, M., Koepke, P., and Schult, I.: Optical Properties of Aerosols and Clouds: The Software Package OPAC, Bulletin of the American Meteorological Society, 79, 831–844, https://doi.org/10.1175/1520-0477(1998)079<0831:OPOAAC>2.0.CO;2, 1998.

Kennedy, J. J., Rayner, N. A., Atkinson, C. P., and Killick, R. E.: An Ensemble Data Set of Sea Surface Temperature Change From 1850: The Met Office Hadley Centre HadSST.4.0.0.0 Data Set, JGR Atmospheres, 124, 7719–7763, https://doi.org/10.1029/2018JD029867, 2019.

Liu, X., Easter, R. C., Ghan, S. J., Zaveri, R., Rasch, P., Shi, X., Lamarque, J.-F., Gettelman, A., Morrison, H., Vitt, F., Conley, A., Park, S., Neale, R., Hannay, C., Ekman, A. M. L., Hess, P., Mahowald, N., Collins, W., Iacono, M. J., Bretherton, C. S., Flanner, M. G., and Mitchell, D.: Toward a minimal representation of aerosols in climate models: description and evaluation in the Community Atmosphere Model CAM5, Geoscientific Model Development, 5, 709–739, https://doi.org/10.5194/gmd-5-709-2012, 2012.

Trenberth, K. E.: The Definition of El Niño, Bull. Amer. Meteor. Soc., 78, 2771–2777, https://doi.org/10.1175/1520-0477(1997)078<2771:TDOENO>2.0.CO;2, 1997.